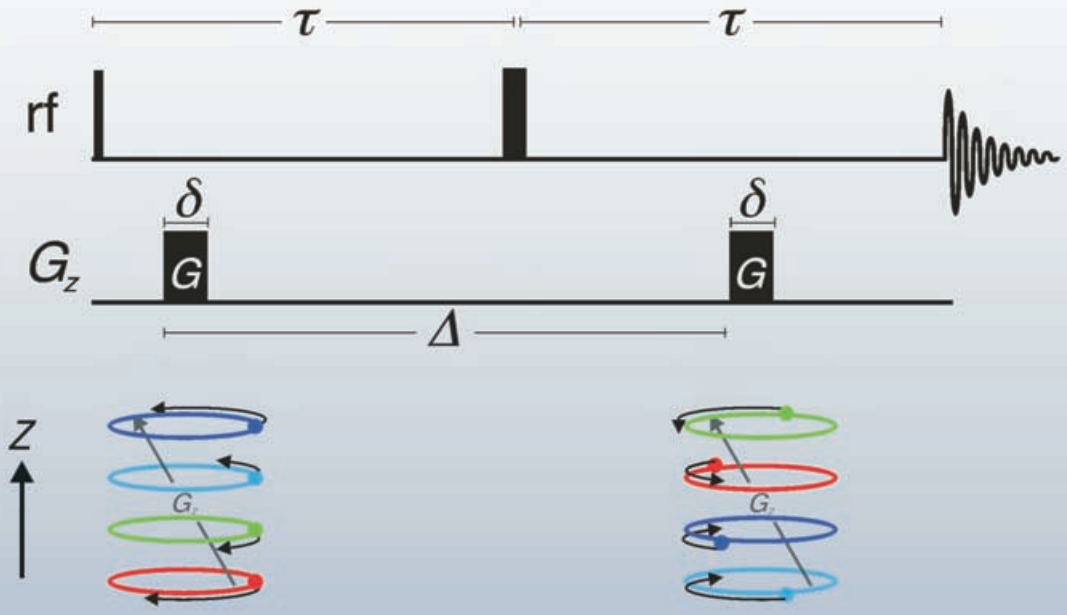

Diffusion NMR Spectroscopy: Folding and Aggregation of Domains in p53

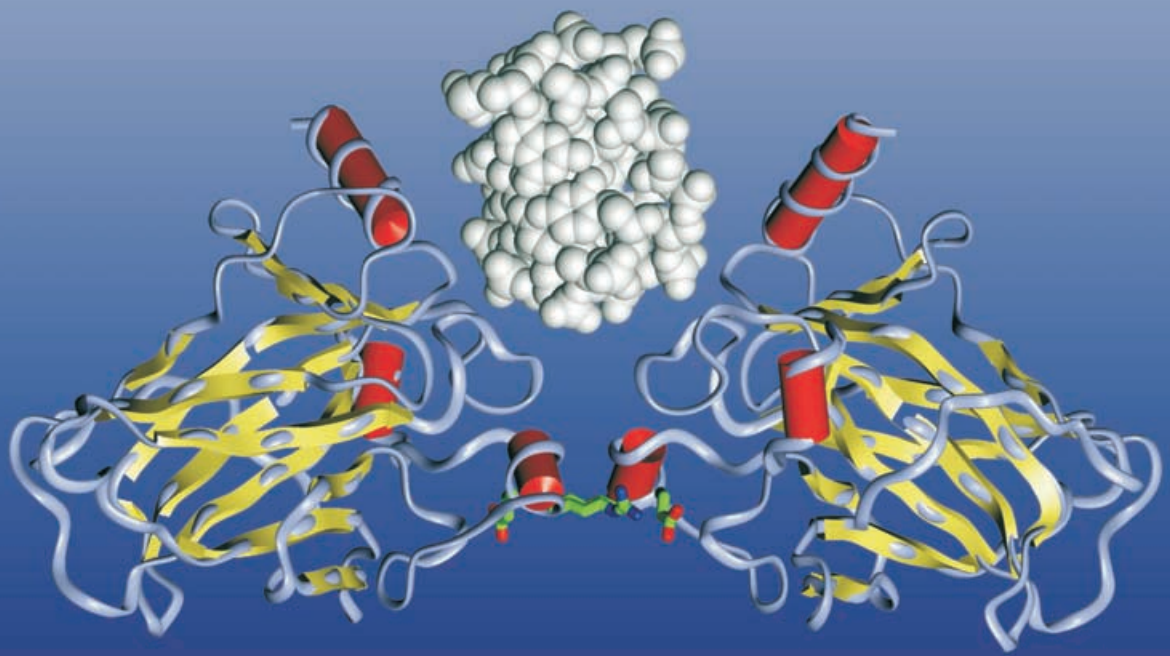

  DOI: 10.1002/cbic.200500093 *ChemBioChem* **2005**, *6*, 1550 – 1565

Diffusion NMR Spectroscopy: Folding and Aggregation of Domains in p53

Alexander Dehner and Horst Kessler*[a]

Protein interactions and aggregation phenomena are probably amongst the most ubiquitous types of interactions in biological systems; they play a key role in many cellular processes. The ability to identify weak intermolecular interactions is a unique feature of NMR spectroscopy. In recent years, pulsed-field gradient NMR spectroscopy has become a convenient method to study molecular diffusion in solution. Since the diffusion coefficient of a certain molecule under given conditions correlates with its effective molecular weight, size, and shape, it is evident that diffusion can be used to map intermolecular interactions or aggregation events. Complex models can be derived from comparison of experimental diffusion data with those predicted by hydrodynamic simulations. In this review, we will give an introduction to pulsed-field gradient NMR spectroscopy and the hydrodynamic properties of proteins and peptides. Furthermore, we show examples for applying these techniques to a helical peptide and its hydrophobic oligomerization, as well as to the dimerization behavior and folding of p53.

Introduction

An understanding of protein function does not end with the identification of the proteins' folds or structures but leads on to an intriguing challenge in modern biology: How do cells respond to, and distinguish between, different stimuli? How does a network of signaling pathways from the membrane to the nucleus transmit environmental changes into a transcriptional response? In fact, protein–protein networks are probably amongst the most ubiquitous types of interactions in biological systems and play a key role in all cellular processes. The determinination of the interaction network of whole organisms has therefore become a major goal of functional genomics efforts. In recent years, hundreds of potentially interacting proteins and their complexes in yeast and other organisms have been identified.[1–8]

In this context, NMR spectroscopy particularly shows its full versatility, as it is not solely a tool for structure determination but can also be applied in a broader manner, thereby combining in a unique fashion the three-dimensional structure, its flexibility, and the identification and characterization of molecular interactions, as well as induced conformational changes. The ability to identify weak intermolecular interactions and structurally characterize them is a unique feature of NMR spectroscopy. Besides chemical shift changes of the target protein induced by ligand binding, there are also other NMR parameters that are commonly exploited in the investigation of protein–ligand binding. When a ligand is bound to a protein, the ligand behaves like the large protein in its dynamic properties: it tumbles more slowly. As a consequence the properties of the protein are transferred to the ligand, thereby resulting in faster relaxation, large and negative NOEs, and slower diffusion.

In the last decade, pulsed-field gradient NMR spectroscopy has become a convenient method for measuring diffusion in solution.[9,10] As the diffusion coefficient of a certain molecule under given conditions is a function of its effective molecular weight, size, and shape, it is evident that diffusion can be used to study intermolecular interactions or aggregation events. Nevertheless, the application of diffusion NMR spectroscopy as a tool for studying molecular interactions only started in the last few years. Gradient NMR spectroscopy is a powerful tool not only for studying diffusion and aggregation; it also provides structure information about cavities in cells or zeoliths in the range of 0.1–100 μm when the diffusion is restricted on the NMR timescale.[11,12] Thus, diffusion can be added to the standard NMR parameters of chemical shift and relaxation times.

In the following review, we give a short theoretical introduction to pulsed-field gradient diffusion NMR spectroscopy, including hydrodynamic calculations that yield "theoretical" values for experimentally determined diffusion coefficients. Finally, we apply these methods in the determination of the hydrodynamic properties of peptides and proteins.

Studying Diffusion by Pulsed-Field Gradient Spin Echoes

There are two ways in which NMR spectroscopy may be used to study self-diffusion: the analysis of relaxation data[13,14] and pulsed-field gradient NMR techniques.[9,10] However, the two methods report motions on rather different timescales. The relaxation method is sensitive to *rotational diffusion*, which is on the picosecond to nanosecond timescale, according to molecular reorientational motions, whereas the pulsed-field gradient echoes measure *translational diffusion* on the millisecond to second timescale.

[a] *Dr. A. Dehner, Prof. Dr. Dr. h.c. H. Kessler*
Department Chemie, Technische Universität München
Lichtenbergstrasse 4, 85747 Garching (Germany)
Fax: (+49) 89-289-13210
E-mail: horst.kessler@ch.tum.de

 DOI: 10.1002/cbic.200500093

In pulsed-field gradient methods, molecular motion is measured by the attenuation of a spin-echo signal due to the dephasing of coherent magnetization, which results from a combination of translational motion of spins (including diffusion, convection, or any other flux) and spatially well-defined gradient pulses.

The basis for diffusion measurements is that magnetic field gradients can be used to label the spatial position of nuclear spins through their Larmor frequency, ω_0, as defined by Equation (1) and given in radians per second, with the gyromagnetic ratio, γ, given in $\mathrm{rad\,T^{-1}\,s^{-1}}$ or $\mathrm{Hz\,G^{-1}}$. B_0 is the strength of the static magnetic field and, since B_0 is spatially homogeneous throughout the sample, ω_0 is the same over the whole sample.

Alexander Dehner, born in 1973 in Villingen-Schwenningen, Baden-Württemberg, studied chemistry at the Technische Universität München where he graduated in 1999. His diploma thesis was on the solution structure, dimerization, and dynamics of a lipophilic $\alpha/3_{10}$-helical peptide studied by NMR spectroscopy. Since 2000 he has been working under the supervision of H. Kessler and he received his PhD degree in 2004. His research interests focus on protein–protein and protein–ligand interactions studied by NMR spectroscopic and biochemical methods.

Horst Kessler was born in 1940 in Suhl, Thuringia. He studied chemistry in Leipzig and Tübingen, where he received his PhD degree for work with Eugen Müller in 1966 and his Habilitation in 1969. He was appointed as full professor for organic chemistry at the J. W. Goethe Universität in Frankfurt in 1971 and moved to the Technische Universität München in 1989. Prof. Kessler is the recipient of the Otto Bayer award (1986), the Max Bergmann medal for peptide chemistry (1988), the Emil Fischer medal (1997), the Max-Planck Forschungspreis (2001), the Vincent du Vignaud Award of the American Peptide Society (2002), the Hans-Herloff-Inhoffen medal, and the Philip Moris Forschungspreis (2003). He is member of the Bavarian Academy of Science and the Leopoldina at Halle and he obtained an honorary doctorate of the University of Leipzig. He has had guest professorships at universities in Halifax, Tokyo, Madison, Haifa, Austin, and Jerusalem. His research activities are in the development and application of NMR methods for the investigation of biomolecules (peptides, drugs, proteins) and their mutual interactions. Another main field of research is drug design and synthesis based on peptides, sugars, peptidomimetics, and drug-like small molecular fragments. Application of integrin ligands for the coating of biomaterials and for the detection of cancer metastasis is another field of recent interest.

$$\omega_0 = \gamma \cdot B_0 \tag{1}$$

If, in addition to B_0, there is a spatially dependent magnetic field, G, given in $\mathrm{T\,m^{-1}}$, the effective ω also becomes spatially dependent, as shown by Equation (2), where p accounts for the possibility of more than a single quantum coherence ($p = 1$) and r is the coordinate vector. G is defined by the gradient of the magnetic field component parallel to B_0, according to Equation (3), where i, j, and k are the unit vectors in the x, y, and z directions, respectively, of the laboratory frame of reference.

$$\omega_{\mathrm{eff}}(p,r) = p(\omega_0 + \gamma(G \cdot r)) \tag{2}$$

$$G = \nabla B_0 = \frac{\partial B_z}{\partial x} i + \frac{\partial B_z}{\partial y} j + \frac{\partial B_z}{\partial z} k \tag{3}$$

If a linear gradient of known magnitude is applied over a defined time period, the Larmor frequency yields an additional phase shift that is dependent on the spatial position of the spin, the direction of the gradient, and the duration and strength of the gradient. In imaging systems, which can produce equally strong magnetic field gradients along the x, y, and z directions [Eq. (3)], it is possible to measure diffusion along any of these directions.[15–17] Moreover, in principle, it is also possible to apply B_1 radiofrequency gradients instead of magnetic B_0 gradients, and the theoretical aspects of this process are analogous.[18–20] In the case of a single magnetic gradient oriented along the z axis parallel to B_0, the magnitude of G is only a function of the position in this direction. Furthermore, from Equation (2) it follows that, the higher quantum transitions are, the more sensitive are the effects of gradients, whereas zero quantum transitions are essentially unaffected by the presence of gradients.

For a single quantum coherence, the cumulative phase shift for a single spin is given by Equation (4). The first term corresponds to the acquired phase shift due to the static B_0 field and the second term belongs to the effect of an applied gradient with duration t. Thus, the degree of additional dephasing of magnetization due to the gradient is proportional to the gyromagnetic ratio, γ, the strength of the gradient, G, the duration of the gradient, t, and the displacement of the spin during the time t in the direction of the gradient, z.

$$\phi(t) = \underbrace{\gamma B_0 t}_{\text{static field}} + \underbrace{\gamma \int_0^t G(t') \cdot z(t') dt'}_{\text{applied gradient}} \tag{4}$$

t' is the first deviation of the gradient duration. The strength of the gradient G may or may not be a function of time: Rectangular gradient pulses are basically constant (see the Pre-emphasis section below); however, under certain circumstances it might be more convenient to apply, for example, sine-shaped gradient pulses, with an obviously time-dependent shape (see the Shaped Gradients section below).

In order to measure translational spin motion, the traditional Hahn spin-echo pulse sequence[21,22] has to be modified:[23–25]

two equal gradient pulses of duration δ are inserted into each delay period (Figure 1, top). This pulse sequence is then called the "Stejskal–Tanner sequence" or "pulsed-field gradient spin-echo (PFG-SE) sequence". In contrast to the steady gradient experiment developed by Hahn, the application of field gradient pulses has a number of substantial advantages:[24] The use of steady gradients during data acquisition yields spectra with considerable line broadening. This can be avoided by using the Stejskal–Tanner sequence and therefore it is possible to measure diffusion coefficients of more than one molecular species simultaneously. Secondly, PFG experiments allow the use of stronger gradients and thus one can measure smaller diffusion coefficients (down to 10–17 $m^2 s^{-1}$). Furthermore, due to the use of pulses, the time in which the measured diffusion takes place is well defined, thereby allowing the effects of diffusion and spin–spin relaxation to be separated. In Figure 1, the Stejskal–Tanner sequence is shown and its effect on the diffusion and flow of the spins is illustrated schematically. A 90° rf pulse is applied which rotates the macroscopic magnetization from its thermal equilibrium in the z axis to the x–y plane. The first gradient pulse of duration δ and magnitude G is applied and the spins experience a phase shift, according to Equation (4). An additional advantage of PFG spin-echo sequences compared to steady gradient-echo pulse sequences is that chemical shifts and frequency dispersions due to residual B_0 inhomogeneities are refocused by the 180° pulse in the middle. The second gradient is equal in magnitude and duration to the first one. Due to the inversion of the phase shifts acquired from the first gradient by the 180° pulse, this second gradient will refocus the magnetization of all the spins dephased by the first gradient, if the spins have not undergone any translational motion with respect to the z axis. However, if the spins have moved during the time period, Δ, between the two gradient pulses refocusing is incomplete, with the degree of remaining dephasing proportional to the average molecular displacement in the direction of the gradients. Thus, in the presence of diffusion, the winding by the first gradient to a "magnetization helix" and the unwinding by the second gradient is scrambled by the diffusion process, thereby resulting in a reduction of coherent magnetization and therefore in a loss of signal intensity. The faster the diffusion occurs, the poorer is the refocusing effect of the second gradient and the smaller is the resulting signal. In the absence of any background gradient, diffusion processes before and after the diffusion delay, Δ, do not affect the signal attenuation. As illustrated in Figure 1, the presence of laminar flow with a constant velocity along the direction of the gradients will yield the same net phase shift for all the spins. If both diffusion and flow are present, the whole diffusion-induced phase shift will receive an additional net phase shift. This flow-induced net phase shift can be compensated for (see the Temperature Gradients and Convection section below),[26,27] by applying the sequence twice with inverted gradient sets.

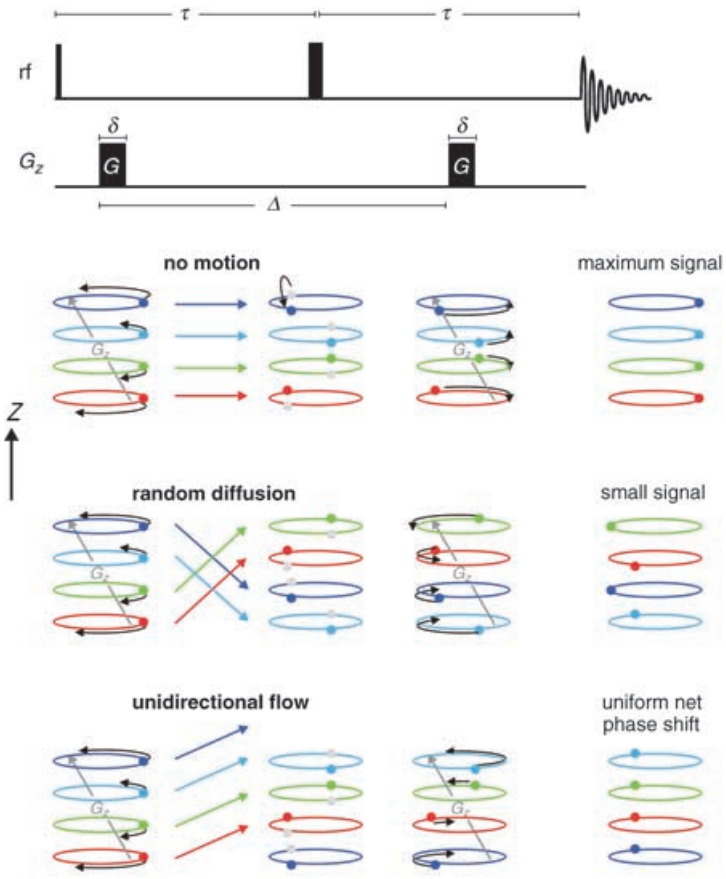

Figure 1. Schematic representation of the Stejskal and Tanner pulse sequence and its effect on the spins due to random diffusion (second row) and unidirectional flow (third row). As only coherent magnetization is observable, random diffusion leads to a loss in signal intensity. In each delay, τ, a gradient pulse of duration δ and magnitude G is inserted. The separation between the gradient pulses is denoted by Δ. Only the precession due to gradients is considered in the rotating reference frame rotating at ω_0.

In addition to the signal attenuation due to diffusion and flow, relaxation processes during 2τ have to be considered. As attenuations due to relaxation and due to diffusion (and flow) are independent, one obtains Equation (5), where S is the signal intensity, T_2 is the transversal relaxation time and $f(\delta,G,\Delta,D)$ represents a function for the attenuation due to diffusion. Hence, if τ is kept constant during all the experiments, the relaxation-induced signal attenuation is constant and can be separated from diffusion-induced attenuation.

$$S(2\tau) = S(0) \cdot \underbrace{\exp\left(-\frac{2\tau}{T_2}\right)}_{\substack{\text{attenuation}\\ \text{due to relaxation}}} \cdot \underbrace{f(\delta,G,\Delta,D)}_{\substack{\text{attenuation}\\ \text{due to diffusion}}} \quad (5)$$

For unrestricted diffusion it is possible to derive the relationship between diffusion and the observed signal attenuation, $f(\delta,G,\Delta,D)$, analytically by using Bloch equations including the effect of diffusion.[28,29] A step-wise time-dependent integration of the Bloch equations for the given pulse sequence yields Equation (6). The resulting exponential signal decay due to diffusion, E, is not a function of the starting point of the first gradient pulse, and therefore the placement of the gradient pulses within the sequence is of no consequence and they do not have to be placed symmetrically around the 180° rf pulse.

$$\ln(E) = -\gamma^2 G^2 \delta^2 D(\Delta - \delta/3) = \ln(f(\delta,G,\Delta,D)) \quad (6)$$

Besides the gyromagnetic ratio, γ, Equation (6) provides three experimental parameters that can be varied during a diffusion measurement: The gradient strength, G, the gradient duration, δ, and the time, Δ, between dephasing and refocusing of magnetization. An increase in one of these parameters will lead to increased signal attenuation. The term $(\Delta-\delta/3)$ is called the diffusion time, where $\delta/3$ accounts for the finite gradient duration. If the Bloch equations are supplemented with an additional term representing unidirectional flow with a constant velocity v, one gets the signal attenuation due to diffusion and flow, as defined by Equation (7).

$$\ln(E) = \underbrace{-\gamma^2 G^2 \delta^2 D(\Delta - \delta/3)}_{\text{attenuation due to diffusion}} + \underbrace{i\gamma\delta G\Delta \cdot v}_{\text{net phase shift due to flow}} \quad (7)$$

While the diffusion results in a loss of echo intensity with an increase in parameters G, Δ, or δ, the flow induces only a phase shift, which is equal for all spins in the sample as long as v is constant and equal for all spins.

The stimulated-echo (STE) sequence

Spin-echo pulse sequences were first studied by Hahn.[21] The effects of diffusion on the stimulated echo (STE) have been studied by using both steady gradients[30] and pulsed-field gradients.[31,32] In Figure 2 the pulse sequence of a standard PFG-STE diffusion experiment is shown. The signal intensity for rectangular gradient pulses, including the effects of relaxation, is given by Equation (8).

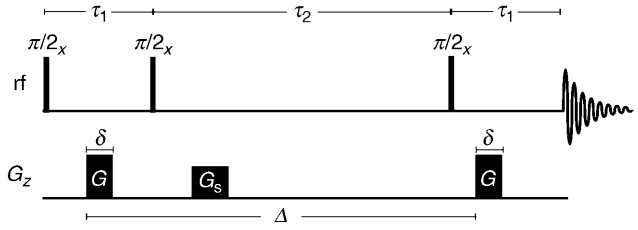

Figure 2. The stimulated-echo (STE) pulse sequence with pulsed-field gradients. During the τ_2 period, magnetization is stored along the z axis and therefore subjected only to longitudinal T_1 relaxation. G_s indicates a spoil gradient.

$$S(2\tau_1+\tau_2) = \frac{S(0)}{2} \underbrace{\cdot \exp\left[-\left(\frac{2\tau_1}{T_2}\right)-\left(\frac{\tau_2}{T_1}\right)\right]}_{\text{relaxation attenuation}} \underbrace{\cdot \exp\left[-\gamma^2 G^2 \delta^2 D(\Delta-\delta/3)\right]}_{\text{Stejskal–Tanner factor}} \quad (8)$$

From Equation (8), it is obvious that the signal amplitude of the PFG-STE experiment is reduced by a factor of two compared to the PFG-SE experiment (Stejskal–Tanner experiment). This is a result of the second 90°$_x$ pulse, which stores the magnetization by rotating only the y components onto the $\pm z$ axis, while the remaining x components are eliminated by phase cycling or spoil gradients (GS). However, the PFG-STE sequence has one major advantage over to the PFG-SE sequence. For most of the time Δ, the magnetization is aligned along the z axis (τ_2 period) and therefore subjected only to longitudinal T_1 relaxation. Since for most macromolecules $T_1 \gg T_2$, the STE sequence is generally preferred over the SE sequence. The ratio of the signal obtained from the stimulated echo sequence compared to that obtained from the Stejskal–Tanner sequence can be calculated by using Equations (5) and (8). With the assumption that $2\tau = T_1$ in the case of the Stejskal–Tanner sequence and $2\tau_1+\tau_2 = T_1$ in the case of the STE sequence, the signal amplitude ratio S(STE)/S(SE) is plotted against the ratio T_1/T_2 in logarithmic scale for three cases: $\tau_1 = \tau_2/2$, $\tau_1 = \tau_2/4$, and $\tau_1 = \tau_2/8$ (Figure 3). For small molecules, $T_1 \approx T_2$ and the stimulated-echo sequence yields half the intensity of the spin-echo sequence. However, if typical values for macromolecules are assumed with $T_1/T_2 \approx 10$, the enhancement factor for the STE sequence is more than 200 and thus easily compensates for the initial 50% loss.

Moreover, large gains in sensitivity and resolution can be made through the use of pulse sequences which generate either homonuclear or heteronuclear multiple quantum transitions. Figure 4 shows as an example a multiple quantum STE pulse sequence. It is the effective sum of the gyromagnetic ratios, γ, of all nuclei involved in the coherence, which is relevant for the attenuation. Hence, the effect of gradients is scaled by p^2, where p is the coherence order; therefore, homonuclear double quantum coherence is four times as sensitive to the effects of field gradients as single quantum coherence.[33] Thus, the attenuation of multiple quantum coherence requires a smaller gradient strength, or smaller diffusion coefficients and differences in diffusion can be distinguished.[34,35] However, in the case of homonuclear coupled spin systems it is important to consider the delays in the pulse sequence with respect to the coupling constant J, in order to obtain a good signal-to-noise ratio. As the in-phase coupling term evolves with a cosine modulation, echo maxima of coupled spin pairs occur when $\tau = n/J$, where n is an integer, and minima occur when $\tau = n/(2J)$. Therefore, in the case of the STE sequence one should keep $\tau_1 \ll 1/(2J)$ with respect to the largest occurring coupling.

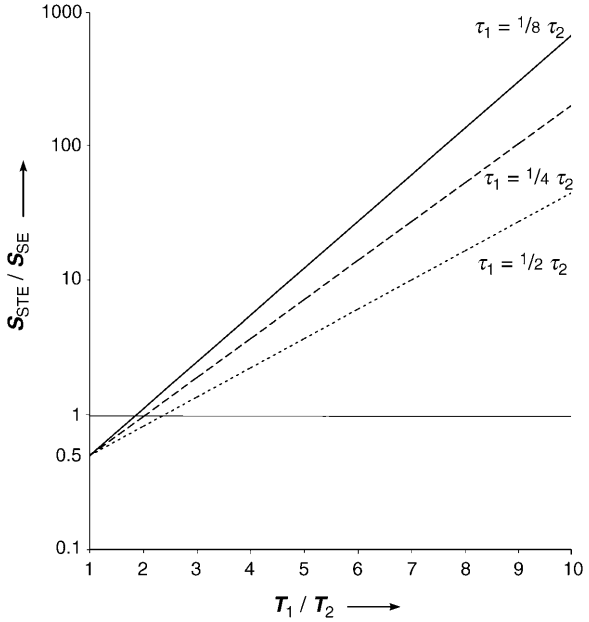

Figure 3. Logarithmic signal ratio of the stimulated-echo (STE) sequence and the Stejskal–Tanner (SE) sequence versus the T_1/T_2 ratio for three cases as indicated. Calculations were performed with the assumption that $2\tau = T_1$ for the SE sequence and $2\tau_1+\tau_2 = T_1$ for the STE sequence. For short T_2 relaxation times in macromolecules, that is, a larger T_1/T_2 ratio, the STE sequence benefits from the τ_2 storage period in which the magnetization is only subject to longitudinal T_1 relaxation.

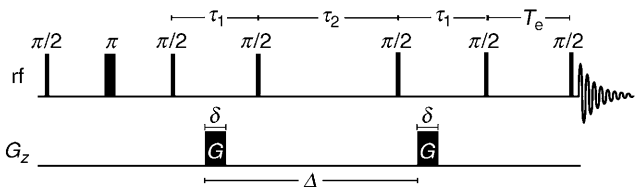

Figure 4. Multiple quantum PFG sequence based on the stimulated-echo experiment. T_e is the eddy-current delay and the phase cycling can be found elsewhere.[33] Relevant for the attenuation is the effective sum of gyromagnetic ratios of the nuclei involved in the coherence, and therefore a multiple quantum PFG experiment is more sensitive to the effects of gradients than a single quantum PFG experiment.

Eddy-current reduction

Rapid changes in gradient pulses can generate eddy currents in surrounding conducting materials. The induced eddy currents and their associated magnetic field interfere with the main magnetic field. They are proportional to the strength of the gradient and are especially caused by rapidly rising and falling gradient pulses, such as rectangular pulse shapes. Their main effect is the delaying of fast changes in gradient amplitude, thereby causing, for example, a "tail" at the end of rectangular gradient shapes (Figure 5). If the eddy-current tail from the first gradient pulse in the Stejskal–Tanner sequence extends into the second τ period, then the total field gradients during the two τ periods are not equal. Thus, even if a spin has not undergone any motion, there will be a residual phase

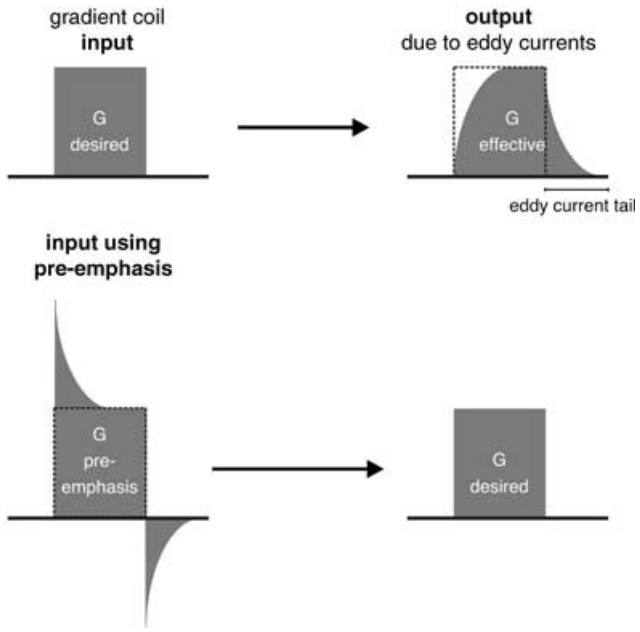

Figure 5. Illustration of the pre-emphasis method. Induced eddy currents in the surrounding material counteract the applied gradient (top). Overdriving the leading and tailing edges of the gradient shape yields the desired shape (bottom).

shift, which will result in phase changes and wiggles in the observed spectra.

Shielded gradient coils: There are several methods of handling eddy-current effects. The most effective solution is to use shielded gradient coils. The commonly used geometries for gradients along the *z* axis are so-called Maxwell pairs of coils which contain one set of windings at either end of the coil in opposite handedness.[36–38] The shielding of this primary gradient coil is achieved by placing a second pair of shielding gradient coils outside the primary one. Therefore, the field outside of the main gradient coil is cancelled, whereas the gradient generated within the sample volume would be largely unaffected by the presence of the shielding coils.[39–41] Typically a reduction of eddy currents to $<1\%$ can be achieved by using shielded gradient coils.[42]

Pre-emphasis: The conceptual idea of pre-emphasis is illustrated in Figure 5. Owing to the generation of eddy currents, input of the ideal waveform into the gradient coil will not produce an identical gradient shape but will result in a distorted waveform. Thus, the input waveform has to be shaped to counteract the eddy-current effects: overdriving the currents at the leading and tailing edges of the gradient pulses will self-compensate for induced eddy-current fields, as the sign of generated eddy fields is opposite to the currents which induce them. This method is called pre-emphasis and is performed by adding small corrections to the desired waveform (Figure 5).[43–45] However, due to the overdriving of currents at the leading and tailing edges of a gradient pulse, this method puts another limitation on the maximum effective gradient strength that can possibly be used. In addition, since the spatial distribution of fields produced by eddy currents is rather different from those generated by the gradient coils, there

is no perfect compensation; however, in combination with shielded gradients, this method further improves the performance.

Longitudinal eddy-current delay (LED) sequence: The major modification in the LED pulse sequence is an additional delay at the end of the pulse sequence,[46] called T_e, which stores the magnetization in the longitudinal direction, while the eddy currents of the second recovery gradient decay (Figure 4). After the period T_e, the magnetization is recalled by a 90° pulse and acquired. However, the LED sequence does not cope with the eddy-current tails of the first gradient. This can be helped by adding a train of three gradient prepulses prior to the actual pulse sequence to yield a train of five equally spaced (Δ) gradient pulses.[47–49] This ensures that the induced magnetic fields, resulting from previous gradients, are equal after the first and third 90° pulse; however, this method also introduces additional heat, which might yield convection artifacts.

Bipolar pulse-pair (BPP) gradients: One of the best solutions to diminish eddy-current effects is the use of self-compensating, bipolar gradient pulses. In this method, the gradient pulse δ is replaced by the composite bipolar gradient combination $(G)180°(-G)$, where G has a duration of $\delta/2$.[50] In Figure 6 the

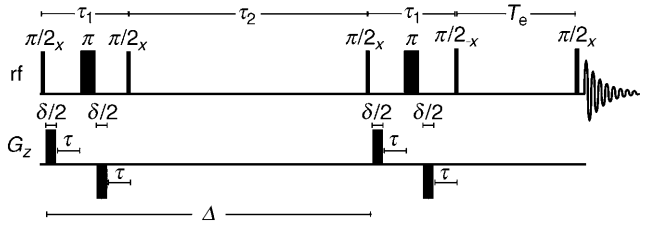

Figure 6. Pulse sequence of the BPP-LED experiment. The self-compensating effect of the bipolar gradient pulse sandwiches largely cancels the generation of eddy currents.

LED sequence is shown with bipolar gradients to encode and decode the magnetization. The two gradient pulses within each bipolar pulse pair are of opposite sign, and the 180° pulse between them inverts the induced phase shifts from the first gradient pulse within the pulse sandwich, such that, taken as a whole, the effective gradient is equivalent to a single gradient pulse of duration δ. While the dephasing effects of both gradient pulses add up, the eddy currents induced by the positive polarity of the first gradient pulse are cancelled by the equivalent negative polarity of the second gradient pulse. Furthermore, the 180° rf pulse prevents an encoding of chemical shifts during the τ_1 period of the STE experiment, which would otherwise reduce the amplitude of the STE signal.[51,52] Originally, gradient pulse sequences with alternating polarity were introduced[53] into PFG NMR spectroscopy in order to take advantage of the refocusing of static magnetic gradients and the effects of background gradients.[54] A potential disadvantage of the BPP-STE or BPP-LED experiment is that the amount of time to complete the composite gradient pulse pair slightly exceeds the time required for a single gradient pulse; thus, when T_2 relaxation times are very short in macromolecular systems, the extra amount of time in transverse magnetization may lead to a loss of signal.[55]

Shaped gradients: The severity of eddy currents is proportional to dG/dt, the rise and fall times of the gradient pulses. Hence reducing eddy currents is possible by slowing down these rise and fall times by using shaped pulses instead of rectangular pulses;[24] those commonly used are sine- or triangular-shaped gradient pulses. The precise shape of the gradient is unimportant for the determination of the diffusion coefficient, as long as the product of gradient strength and gradient duration (that is, the integral running over the gradient's shape) is equal to that of the ideal rectangular pulse.[56] A detailed discussion and derivation can be found elsewhere.[9,56] However, the ratio of $G\delta$ between a rectangular and a sine-shaped gradient is $2/\pi$, and for a squared-sine shape this ratio is 0.5. Thus, compared to a rectangular gradient pulse of duration δ, a sine-shaped gradient pulse applies an effective gradient $G\delta_{sine}$ that is reduced by a factor of $2/\pi$, and the effective gradient of a squared-sine shape is reduced by 0.5. This has to be taken into account when the data of a diffusion experiment are analyzed, for example, in a nonlinear least squares regression of the exponential signal decay against the gradient strength.

Temperature gradients and convection

Convection currents are induced in nonviscous samples by temperature gradients. These temperature gradients can easily occur along the z axis, since temperature regulation in NMR probes is normally performed by flowing heated or cooled nitrogen gas through the base of the probe. With the assumption that the induced convective compensation currents are planar along the z axis, the convection will transport equal amounts of sample in opposite directions along the temperature gradient. As already outlined above (Figure 1), unidirectional flow will cause a net phase shift which is equal for all the spins in the sample; however, convection is, considering the z axis only, a bidirectional flow with a distribution of velocities. Therefore, convection causes a corresponding damping factor, which results from a vector addition of positive and negative phase changes that interfere with the attenuation due to diffusion and thus increase the apparent diffusion coefficient. In addition, a nonexponential signal decay can be observed:[57] for longer Δ diffusion times, one can observe an increasing oscillation of the signal amplitude. Actually, the measured diffusion coefficient should be independent from the chosen diffusion time and, therefore, this oscillation is a sensitive detector for the existence of convection artifacts.

The double-stimulated spin-echo experiment: As already outlined, these convection artifacts can be compensated for by "applying the sequence twice" with inverted gradient sets. This method relies on gradient moment nulling and means that a second gradient set of opposite effective polarity is applied during the sequence, thereby inducing an opposite handedness of the "magnetic helix". Therefore, an opposite net phase shift compared to that of the first gradient is achieved and

cancels acquired phase shifts, thereby leaving the diffusion process only. The mathematical requirement is that the first moment of effective gradients G^* over the entire pulse sequence is zero, with p being the coherence order [Eq. (9)].[58]

$$\int_0^t G_z^*(t')dt' = 0 \qquad (9)$$

where $G_z^* = p \cdot G_z$

Figure 7 illustrates the most simple velocity-compensated gradient sequence, where during the first half (2δ) the magnetic winding is of opposite handedness to that in the second half and the overall first moment over all gradients is zero. The

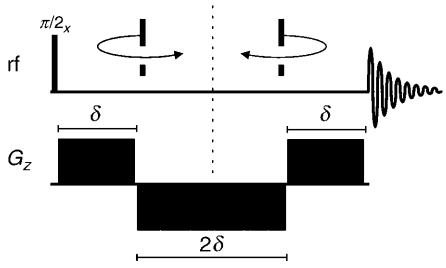

Figure 7. Simple gradient spin-echo pulse sequence with a zero first moment of the gradients. The handedness of magnetic winding is indicated above the sequence. Zero first moment gradient sequences are used to refocus net phase shifts induced by flow.

flow-compensated double stimulated-echo sequence as proposed by Jerschow and Müller[26] is shown in Figure 8, with bipolar gradients and an eddy-current delay at the end of the sequence, which also allows both coherence-transfer pathways of opposite signs during the precession period to be converted into observable magnetization. The first moment of the effective gradient over the whole sequence is zero and the winding during each diffusion period $\Delta/2$ is of opposite handedness and therefore refocuses all constant velocity effects. A proper coherence pathway selection, as indicated in Figure 8,

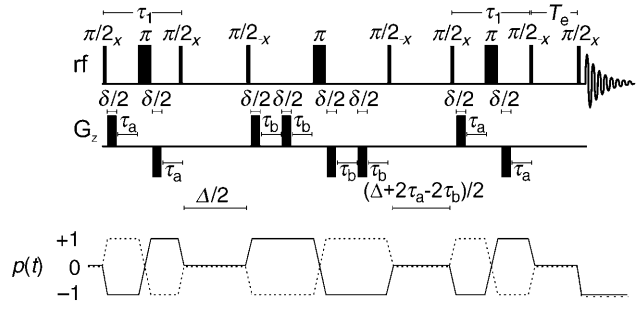

Figure 8. Double stimulated spin-echo experiment with bipolar gradient pulses and an eddy-current delay, T_e, at the end of the sequence. τ_a and τ_b are gradient recovery delays. The selected coherence transfer pathways, $p(t)$, are given beneath the sequence. Bidirectional flow yields an additional attenuation of the signal amplitude. However, the whole sequence has a zero first moment of gradients and thus compensates for (bidirectional) flow-induced signal attenuations.

is essential, because the effective gradient is proportional to the coherence order [Eq. (9)]. The gradients in the center of the double stimulated-echo experiment might be merged together; however, due to different rise and fall times, discrete identical gradients, such as those during τ_1, yield better refocusing. Since chemical shifts are refocused separately in each precession period by 180° pulses, the delays τ_a and τ_b need not be equal.

Effects of chemical exchange

Chemical exchange processes are defined by their rate relative to the NMR timescale. They can be grouped into *slow exchange*, which is defined by a situation where characteristic individual sites can be observed in the spectra by individual signals, and *fast exchange*, which yields a time-averaged spectrum over the different sites. The path from slow exchange to fast exchange consists of line broadening, coalescence, and motional narrowing as the mean lifetimes for the occupation of different sites decrease. These exchange rates, that is, the inverse lifetimes, can be manipulated by changes in temperature or concentration of participating species for intermolecular interactions.[59,60] Diffusion NMR spectroscopy is able to observe chemical exchange between species with different hydrodynamic properties, for example, a small ligand binding to a larger protein. Under favorable conditions it is possible to obtain a diffusion spectrum with two individual peaks within the slow-exchange limit and similarly a diffusion spectrum with a single peak within the fast-exchange limit. This can be controlled by a variation of the storage time, τ_2, in STE-type diffusion experiments without changing the physical properties of the sample.[52,61] Figure 9 illustrates the effect of different τ_2 storage times on the stimulated echo amplitude for a two-site

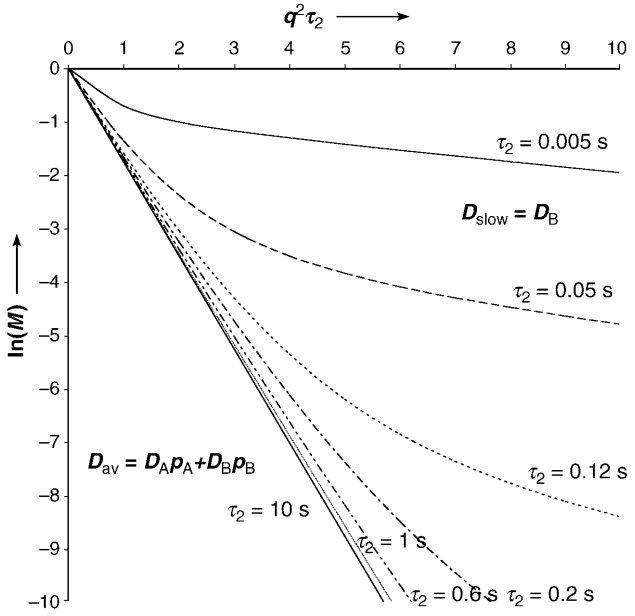

Figure 9. Effects of the logarithmic echo amplitude ln(M) versus the "gradient effect", $q^2\tau_2$, for a two-site exchange. In performing these simulations it is assumed that $D_A = 2.0$, $D_B = 0.1$, $k_A = 10$, $k_B = 66.6$, $M_{A0} = 0.4$, and $M_{B0} = 0.6$.

exchange. A logarithmic plot of the signal decay ln(M) versus $q^2\tau_2$ is shown, where q is the "gradient effect", defined by $q=\gamma G\delta$. The slow-exchange limit is represented in the upper curves for small values of τ_2. The dominating effect of these curves is basically the summation of two exponentials and thus the slope is associated with both diffusion coefficients, D_A for the free ligand and D_B for the protein-bound ligand. Within the limit of large $q^2\tau_2$ values (for example, a strong gradient strength), D_{slow} dominates, which corresponds to D_B, whereas the initial slope for small values of $q^2\tau_2$ (for example, a weak gradient strength) yields the fast-exchange limit which corresponds to a population-averaged diffusion constant $D_{av}=p_AD_A+p_BD_B$, where p is the population. Therefore, it is also possible to extrapolate the populations A (free ligand) and B (protein-bound ligand) in a two-site exchange, because the intercept at $q^2\tau_2=0$ of the line with slope D_{av} is taken to be $\ln(M_A+M_B)$, while the intercept of the slow-exchange line extrapolated from large $q^2\tau_2$ values is equal to $\ln(M_B)$. The curve with the steepest slope, actually a straight line with slope D_{av}, represents the fast-exchange limit, which can be obtained by setting the storage period τ_2 to be so long that the mean number of times that a spin changes sites is higher than 10. The application of this theory for the analysis of protein–ligand interactions is called affinity NMR spectroscopy[62] and an example is given by Derrick et al.[52,63]

Diffusion-ordered spectroscopy (DOSY)

One of the most important applications of pulsed-field gradient diffusion NMR spectroscopy is diffusion-ordered spectroscopy (DOSY). The DOSY technique separates signals within a compound mixture according to their translational diffusion coefficients. Thus, it is possible to analyze mixtures without a prior physical separation, for example, by chromatography. The principle idea of DOSY is analogous to conventional multidimensional NMR spectroscopy: Diffusion spectra can be obtained by incrementing the "gradient effect" reflected in the value of $q=f(\gamma)G\delta$. These data sets can be represented by a weighted sum of Stejskal–Tanner factors,[24] where N is the number of compounds within the mixture, $A_i(\nu)$ is the initial spectrum of the ith compound without applied gradients, and D_i is its diffusion coefficient [Eq. (10)].

$$f(q,\nu)=\sum_{i=1}^{N} A_i(\nu)\cdot\exp\{-D_i\cdot q^2\cdot(\Delta-\delta/3)\} \qquad (10)$$

Approximate inverse Laplace transforms (ILTs) of the signal amplitude with respect to q^2 yield the second dimension of a spectrum that correlates the chemical shift with its diffusion coefficient, a so-called DOSY spectrum.[55,64] However, unlike the Fourier transformation of an FID, which yields a unique NMR spectrum, the inverse Laplace transformation (ILT) of the decay function is often not unique and a number of reasonable assumptions have to be made. Different software packages dealing with this problem have been described in the literature, such as DISCRETE,[65,66] SPLMOD,[67] CONTIN[68] and MaxEnt,[69] and a review of available software has been given by Johnson.[55] The third or second axis in a DOSY spectrum is not a chemical shift but a diffusion dimension (Figure 10).[70] Any 2D NMR experiment can be used in this combination and Figure 11 illustrates a 3D COSY-DOSY sequence.[71] Other combinations such as HMQC-[72] or HSQC-DOSY,[73] TOCSY-DOSY,[74] and NOESY-DOSY[75] have been reported in the literature.

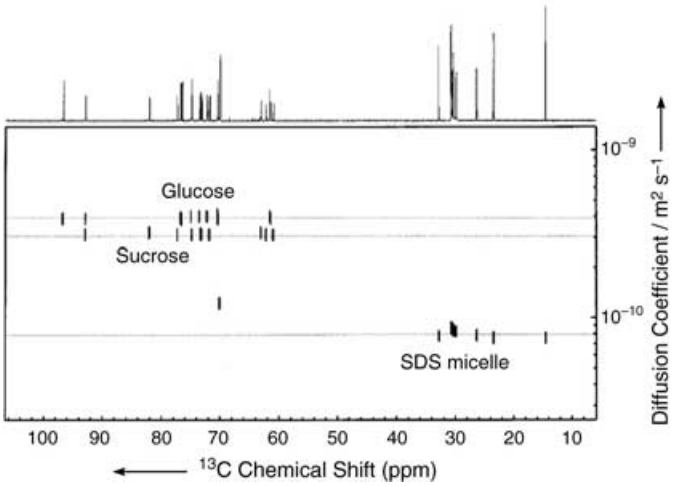

Figure 10. ^{13}C-INEPT DOSY plot for a mixture containing glucose, sucrose, and sodium dodecylsulfate (SDS) in D_2O. Each dotted line represents the average diffusion coefficient of the individual component. On top of the 2D display the 1D ^{13}C-INEPT spectrum is shown.[70]

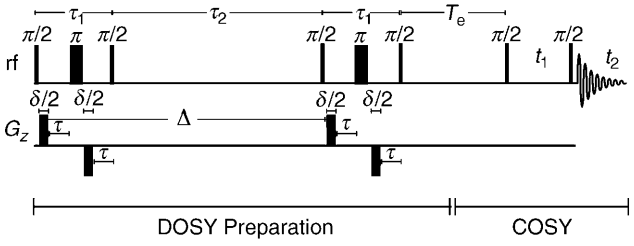

Figure 11. Pulse sequence for the 3D DOSY-COSY experiment. The phase cycling is given in ref. [71].

Hydrodynamic calculations

Translational diffusion is one of the most important modes of molecular transport. Brownian motion in the absence of an applied force is the origin of self-diffusion; in this case, no external force acts on the molecular particles and, consequently, no net displacement is observed. However, external fields can be applied to force additional translational motion. These fields include gravity or angular acceleration in sedimentation or ultracentrifugation experiments and electric fields in electrophoresis.[76–78] With the assumption that all solute molecules are moving with the same average velocity $<v>$, the flux J across a surface element will be $J=c<v>$, where c is the concentration. A molecule moving in this way will feel a total frictional force given by $<v>f$, where f is the translational friction,

which must be opposed by an equal force if there is no net acceleration. As known from Fick's first law of diffusion, concentration gradients produce a diffusion force that leads to molecular transport of the solute. Thus, in the case of free diffusion, where no external forces are applied, the diffusion force and the frictional force can be set as equal. In doing so, one arrives at the so-called Einstein–Sutherland equation [Eq. (11)].

$$D = -\left(\frac{kT}{f}\right) \cdot \left(1+\frac{\partial(\ln \gamma_2)}{\partial(\ln c_2)}\right) \quad (11)$$

In an infinite dilution, the activity coefficient γ_2 of the solute molecules becomes 1.0; therefore, the differential $\partial(\ln \gamma_2)/\partial(\ln c_2) = 0$ and the diffusion constant D_0 at infinite dilution is defined by Equation (12).

$$D_0 = -(kT/f) \quad (12)$$

Thus, the diffusion constant of a molecule will be a function of the temperature and it will also depend on the solvent viscosity, as the translational friction f is proportional to the radius of the diffusing particle r and to the solvent viscosity η, which is itself a function of temperature. For molecular species of different geometries, different approaches are needed to describe the hydrodynamic frictional coefficient, f. If a spherical (sph) particle interacts strongly with the fluid molecules, resulting in strong frictional forces, one obtains the so-called Stokes law under sticky boundary conditions [Eq. (13)].

$$f_{\text{sph,sticky}} = 6\pi \cdot \eta \cdot r \quad (13)$$

Most macromolecules of biological interest are not spheres but appear to be compact, globular or irregular rigid bodies, and therefore an ellipsoid (eli) is a more realistic model. For equal volumes, the surface area of an ellipsoid is larger than that of a sphere, so it follows that ellipsoids will have larger frictional coefficients than the equivalent spheres. The dependence of the frictional coefficient of an ellipsoid on the axial ratio $p_r = a/b$, where a and b are the long and short semiaxes, respectively, can be calculated for sticky boundary conditions. For a prolate ellipsoid this yields Equation (14).

$$\mathrm{F} = \frac{f_{\text{eli}}}{f_{\text{sph}}} = \frac{\sqrt{1-p^2}}{\sqrt[3]{p^2} \cdot \ln\{[1+\sqrt{1-p^2}]/p\}} \quad (14)$$

$$p = b/a = 1/p_r$$

The translational frictional coefficient ratio F is often called a shape factor or Perrin factor. With increasing axial ratio, this factor increases gradually. Equation (14) indicates that a measured self-diffusion coefficient of a given molecular species under controlled conditions, for example, free isotropic diffusion, in principle, provides information on the effective size or weight of a diffusing species; even though a single value of F is consistent with many possible shapes, it is sensitive to structural properties.

Unfortunately, real solutions do not show such a simple behavior, as proteins interact with a substantial number of water molecules. The term hydration refers to effects ranging from specific entrapment of structural water molecules in internal cavities, for example, as observed in crystal structures, to the generic perturbation of the water layer covering the external protein surface. Protein–water interactions play an essential role for the folding, stability, and function of proteins. Since the primary events of biological processes, such as enzymatic catalysis, association, and recognition, take place at the protein–water interface, the dynamics of the hydration layer is of special interest. Much of the experimental information about protein hydration dynamics has come from NMR relaxation experiments[79,80] and protein–water intermolecular NOEs.[81,82] This inner hydration sphere interacts and will move with the protein; it will therefore contribute to the protein's apparent size and also alter its hydrodynamic properties. Different classes and spheres of bound water are merged together into a net weight of bound water per weight of macromolecule, if it is assumed that water occupies all internal spaces and covers the surface of the macromolecule. The hydrated radius of an equivalent sphere, r_h, can then be calculated from the hydrated volume, V_h, by use of Equation (15), where V_2 and V_1 are the partial specific volumes of the macromolecule and the solute, respectively, and δ_1 is the hydration given in grams of bound water per gram of macromolecule.[78]

$$V_{\mathrm{h}} = (M/N_{\mathrm{A}})(\bar{V}_2+\delta_1\bar{V}_1) \quad (15)$$

Therefore, if the shape is already known independently, for example, from electron microscopy or X-ray crystallography, then measured frictional coefficients can either yield the molecular weight and consequently the molecule's possible aggregation state or yield the hydration, if the other quantity is available independently or can be estimated in terms of a model.

The hydrodynamic behavior of macromolecules in solution can be calculated and simulated by starting from the atom coordinates of a given molecule. The macromolecular properties that can be obtained from hydrodynamic calculations are translational diffusion coefficients, D_t, rotational diffusion coefficients, D_r, relaxation times, τ, the intrinsic viscosity, η, and the radius of gyration, R_g. From one or more properties it is possible to determine the size and shape of possible protein aggregations, their anisometry (axial ratio), and the degree of hydration. The problem of predicting the hydrodynamic properties of rigid macromolecules of arbitrarily complex shape was first studied by Bloomfield et al.[83,84] They used simple models of identical elements[85] and devised procedures for calculating the properties for models composed of equal or unequal spherical elements, the so-called beads. There are different strategies for building the hydrodynamic bead model; a review of these different modeling approaches and their advantages and disadvantages is given by García de la Torre et al.[86] In general, a bead model is any representation of a particle as an array of spherical frictional elements. Individual Stokes law friction coefficients are assigned for each element, and the hydrodynamic interaction between them is taken into account. For a particle of arbitrary shape, the hydrodynamic resistance is expressed by means of a 6×6 friction tensor, Ξ, and the Browni-

an diffusion is expressed similarly by a 6×6 diffusion matrix, *D*. The friction forces must be compensated for by the averaged kinetic energy of the particle, and thus, according to the Einstein equation, the diffusion tensor is inversely proportional to the friction tensor [Eq. (16)].[87]

$$D = kT/\Xi \qquad (16)$$

The theory of hydrodynamic properties of bead models provides a procedure for the calculation of the components of Ξ. A key concept in bead model hydrodynamics is the hydrodynamic interaction effect. The frictional force experienced by a bead depends not only on its relative velocity and its friction coefficient but also on the frictional forces that act on all the other beads. This is accounted for by 3×3 hydrodynamic interaction tensors, $T_{ij}(i,j=1,\ldots, N)$, between beads *i* and *j*, where *N* represents the number of beads used in the model.[88]

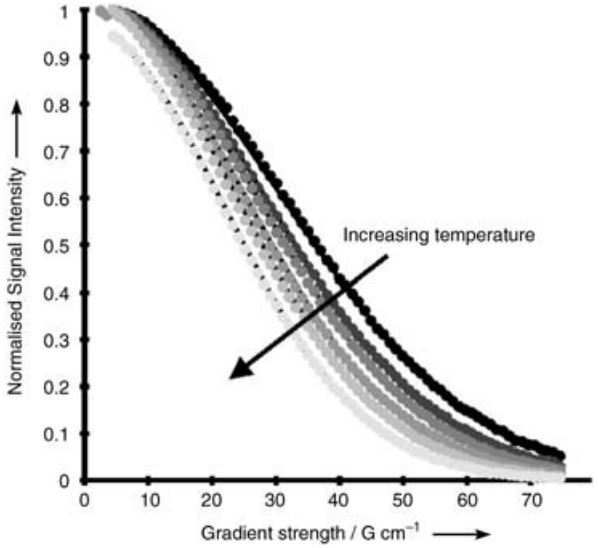

Figure 12. Temperature-dependent signal decay of the heptapeptide *m*BrBz-Iva1-Val2-Iva3-(αMe)Val4-(αMe)Phe5-(αMe)Val6-Iva7-NHMe observed by using a pulsed-field gradient echo diffusion experiment with suppression of convection artifacts. $T = 273$ K, diffusion constant $D = 2.11\times10^{-10} \pm 8.3\times10^{-12}$ m^{2}s^{-1}, $T = 280$ K, $D = 2.53\times10^{-10} \pm 5.6\times10^{-12}$ m^{2}s^{-1}, $T = 285$ K, $D = 2.78\times10^{-10} \pm 3.5\times10^{-12}$ m^{2}s^{-1}, $T = 290$ K, $D = 3.17\times10^{-10} \pm 8.1\times10^{-12}$ m^{2}s^{-1}, $T = 295$ K, $D = 2.56\times10^{-10} \pm 1.4\times10^{-12}$ m^{2}s^{-1}, $T = 300$ K, $D = 3.93\times10^{-10} \pm 1.5\times10^{-12}$ m^{2}s^{-1}. Reprinted with permission from ref. [93]. Copyright (2001) American Chemical Society.

Oligomerization and Hydrodynamic Properties of Peptides and Proteins

Application to lipophilic interactions: Antiparallel dimerization of a helical peptide

It is well documented that peptides rich in Cα-methylated α-amino acids such as α-aminoisobutyric acid (Aib) or isovaline (Iva) have a tendency to adopt either the 3_{10}- or the α-helical conformation in the crystalline state, as well as in structure-supporting solvents.[89–92] Investigations on the 3_{10}/α-helical equilibrium in chloroform solution of the lipophilic heptapeptide *m*BrBz-Iva1-Val2-Iva3-(αMe)Val4-(αMe)Phe5-(αMe)Val6-Iva7-NHMe (*m*BrBz = *meta*-bromobenzoyl, (αMe)Val = Cα-methylvaline, (αMe)Phe = Cα-methylphenylalanine), by NMR spectroscopy revealed a dimerization behavior of the peptide due to favorable van der Waals interactions, in the sense of shape complementarity such as a bulge fitting into a groove.[93,94] In fact, the NOESY spectrum showed a few intermolecular NOEs, especially from the amide proton of Val2 to the C-terminal blocking group NHMe and from side chain to side chain, which could indicate either an antiparallel side-by-side aggregation or a head-to-tail aggregation, as described in the crystal structure of Boc-Val-Ala-Leu-Aib-Val-Ala-Leu-(Val-Ala-Leu-Aib)$_2$-OMe (Boc = *tert*-butyloxycarbonyl).[95] This aggregation phenomenon was studied further by temperature-dependent diffusion measurements on the heptapeptide. Temperature-dependent spin-echo diffusion measurements were performed with 6 steps in the range of 273–300 K by using the double stimulated-echo experiment (Figure 8), which yields a suppression of convection artifacts (Figure 12). The diffusion coefficients were calculated by applying a nonlinear least squares regression to the signal decay according to the Stejskal–Tanner factor [Eq. (6)]. The calculated self-diffusion coefficient of $CHCl_3$ was used as an internal standard. In order to estimate the hydrodynamic radius of the heptapeptide in a saturated $CHCl_3$ solution, the Stokes–Einstein equations [Eqs. (12) and (13)] were used by taking into account the temperature dependence of the dynamic viscosity of $CHCl_3$ and a friction factor for the helical shape of $f/f_0 = 1.04$. With the assumption of a helical geometry for the heptapeptide, as indicated by the NOESY spectrum, the hydrodynamic diameter of the monomeric helix is 15.5 Å. For an antiparallel side-by-side aggregation, the hydrodynamic diameter should increase to about 1.5 times that of the monomeric helix. Therefore, the evaluated hydrodynamic ratios between 2.3 ± 0.1 at 273 K and 1.8 ± 0.1 at 300 K clearly indicate at least a dimerization. The calculated dimer structure is shown in Figure 13 as a space-filling Connolly surface of each monomer and is held together by favorable lipophilic interactions. Karle has shown by X-ray diffraction structures of helical peptides that the dominating factor of packing motifs in apolar helices is not their dipolar nature but rather a shape selection,[95] such as a bulge fitting into a groove. Thus, shape complementarity is essential for molecular recognition of the apolar helices. The studied heptapeptide can be considered as a model for two relevant aspects of transmembrane protein folding. According to the two-stage model[96] or the diffusion collision model,[97] there is first a build-up of stable local structural elements, for example, helical geometry, which is responsible for the formation of a specific molecular shape; secondly, this shape is recognized as attractive by other surrounding structures, thereby yielding a complex of higher order.

Electrostatic interactions: p53 DNA-binding domain (DBD) dimerization behavior

The p53 protein is a transcription factor regulating many cellular processes, including the cell cycle, DNA repair, programmed

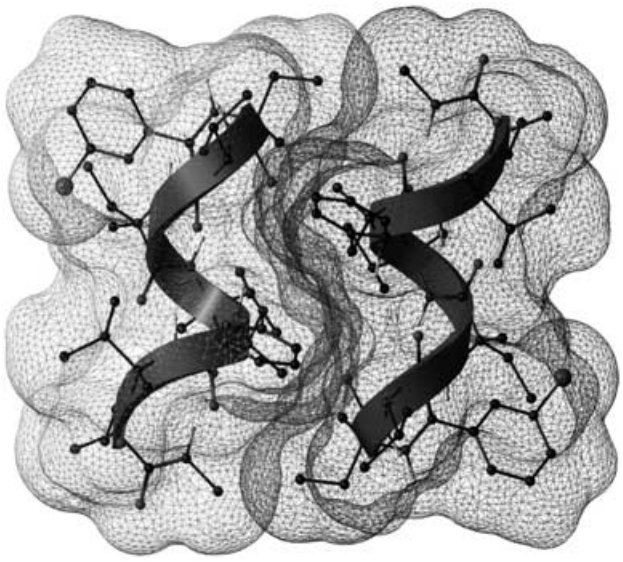

Figure 13. Dimeric structure of the heptapeptide *m*BrBz-Iva1-Val2-Iva3-(αMe)Val4-(αMe)Phe5-(αMe)Val6-Iva7-NHMe showing the antiparallel side-by-side aggregation in the sense of a bulge fitting into a groove, depicted with a van der Waals surface. Reprinted with permission from ref. [93] Copyright (2001) American Chemical Society.

cell death, angiogenesis, and senescence, and it thus acts as a major tumor suppressor.[98–102] The induction of apoptosis by transcriptional activation of proapoptotic target genes in response to cellular stress or DNA damage is the most conserved function of p53, which prevents an accumulation of mutated genome.[103] Therefore, DNA binding is crucial for its tumor suppression function and this is a highly cooperative process in solution.[104–109] This cooperativity in DNA binding, even in the absence of the tetramerization domain, implies the existence of core–core interactions. At present no structural information is known about full-length p53 and its tetrameric organization bound to DNA, yet several reports discuss inter-domain contacts in p53[109–114] based on modeling of the individual structures of the p53 DBD[111,114] and the tetramerization domain.[115–117] NMR chemical shift perturbation experiments of ^{15}N-labeled p53 DBD and consensus oligonucleotide suggest an essential role of the short H1 helix (Pro177–Cys182) for intermolecular p53 DBD dimerization.[106,118] A mutational study of solvent-exposed residues within the H1 helix dimerization interface of the p53 DBD indicated the existence of two intermolecular Glu180–Arg181 salt bridges. This was examined by pulsed-field gradient diffusion NMR spectroscopy, as well as other techniques such as electrophoretic mobility shift assays and fluorescence anisotropy measurements. The following dimerization mutations were introduced by site-directed mutagenesis: H178A, R181A, C182A, E180R, and R181E. One double-site mutation, E180R/R181E, was also introduced. All of these mutations are located within the H1 helix region. As solvent-exposed residues and their side chains do not have an impact on the structural integrity of the p53 DBD, all H1 helix dimerization mutants should be natively folded, which was investigated by NMR spectroscopy. Figure 14 shows an overlay of the ^{15}N-HSQC spectra of all six mutants and wild-type p53 DBD, thereby proving that all the dimerization mutants are indeed natively folded. Addition of consensus oligonucleotide to wild-type p53 DBD causes a reduction of 27.1% in the diffusion coefficient of p53 DBD (Figure 15) as measured by pulsed-field gradient NMR spectroscopy. This is due to cooperative binding of two p53 DBDs to one decameric half-site consensus oligonucleotide. The measured value is in good agreement with hydrodynamic calculations performed by using the shell model of HYDRONMR[119] and a dimeric p53 DBD–DNA model complex as described by Klein et al.,[106] which results in a theoretical reduction of the diffusion coefficient of about 33%. The monomeric p53 DBD–DNA complex (PDB code: 1TSR; chain B including the DNA) was also used for hydrodynamic calculations yielding a reduction compared to free p53 DBD of only 18% upon DNA binding. Thus, these two theoretical values represent the range expected for an equilibrium of monomeric and fully cooperative DNA binding. Deviations from the values of the two borderline cases reflect an averaging of higher and lower oligomeric states. Figure 15 illustrates the reduction of the diffusion coefficient upon addition of 0.6 equivalents of

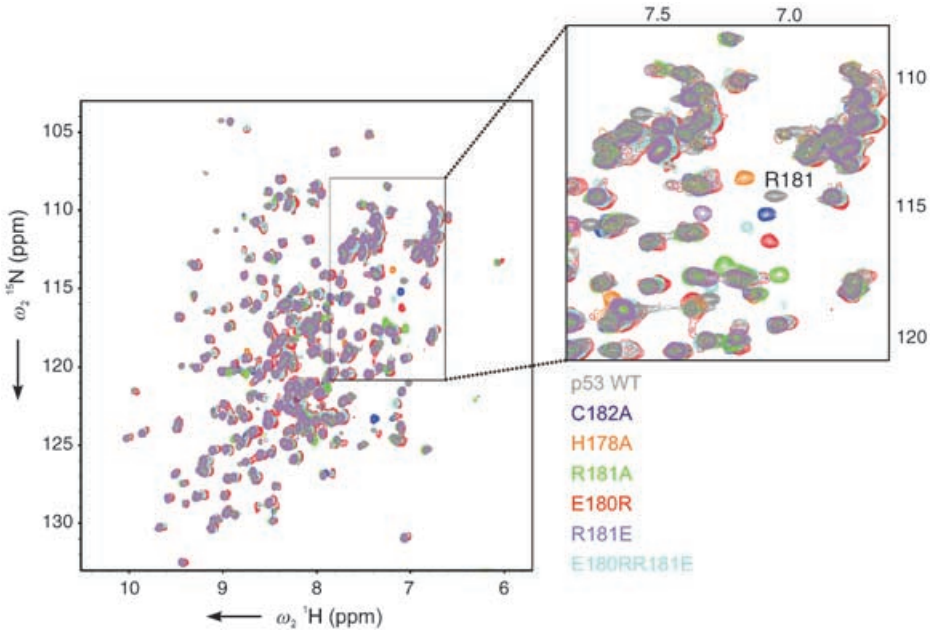

Figure 14. Superposition of the ^{15}N-HSQC spectra of p53 DBD wild-type (grey) and six mutated p53 DBDs. The enlarged section shows residue Arg181 within the H1 helix. Adapted from ref. [135].

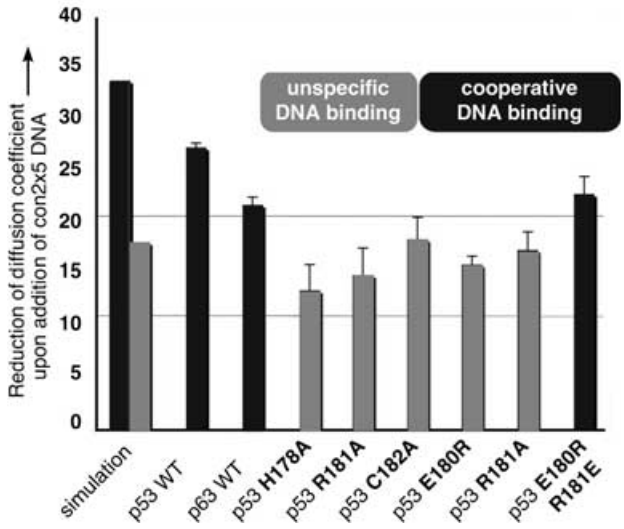

Figure 15. Reduction of the diffusion coefficients of p53 DBD, p63 DBD, and the p53 DBD dimerization mutants upon complexation with consensus DNA, as measured by pulsed-field gradient NMR spectroscopy. Hydrodynamic simulations with a cooperative p53 DBD–DNA model predict a theoretical reduction of 33%, while a single-site binding of DNA should result in 18% reduction. Adapted from ref. [135].

CON2x5 half-site oligonucleotide to achieve a stoichiometric 1:2 DNA/p53 DBD ratio of wild-type DBDs of p53 and p63 and the various p53 DBD dimerization mutants. As already indicated by ^{15}N-HSQC titration, all mutants bind to DNA to result in a reduction of the diffusion coefficient of at least 13%. It can be concluded that p53 DBD wild-type and the double-site mutation E180R/R181E have a similar tendency to bind DNA cooperatively, whereas this tendency is less pronounced for the single-site mutations H178A, R181A, C182A and E180R, and R181E. These results were corroborated by electrophoretic mobility shift assays and fluorescence anisotropy measurements. Taken together, all these results support the idea that the proposed additional dimerization interface of p53 DBD in stabilizing a cooperative and selective binding to DNA consists mainly of two intermolecular Glu180–Arg181 salt bridges from each monomer to the other (Figure 16). These salt bridges are in agreement with a C_2 symmetric complex as proposed by Klein, Lebrun, and their respective co-workers[106, 112] and they rationalize the different DNA-binding behaviors of p53 DBD and p63 DBD.

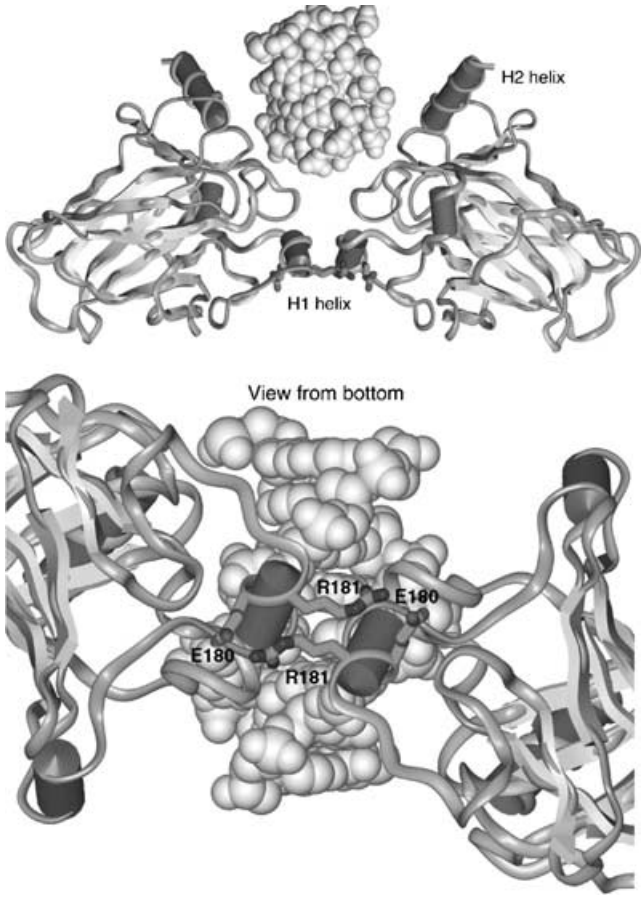

Figure 16. C_2 symmetric complex modeled on the identified dimerization interface of p53 DBD upon cooperative DNA binding. The dimerization interface is stabilized by a double intermolecular salt bridge between the Glu180 and Arg181 residues. Adapted from ref. [135].

PFG NMR spectroscopy reveals a natively unfolded N-terminal domain of p53

To gain further insight into the conformation of the N-terminal domain of p53 (Np53; residues 1–93), we analyzed its structure at pH 7.5 and 298 K by NMR spectroscopy. As shown in Figure 17, only a small proton resonance dispersion in the spectral range of $\delta = 7.5$–8.7 ppm is observed in the ^{15}N-HSQC spectrum, which is characteristic for a highly unfolded protein. In addition, the seven NH_2 side-chain signals of the asparagine and glutamine residues accumulate in their characteristic random-coil region of $\delta = 7.59/6.88$ ppm. The same characteristic was observed for the side-chain signals of the three tryptophans of Np53, which appear at $\delta = 10.2$ ppm. Taken together, the spectrum shows on the amino acid level that residues 1–93 of p53 are mostly unstructured.

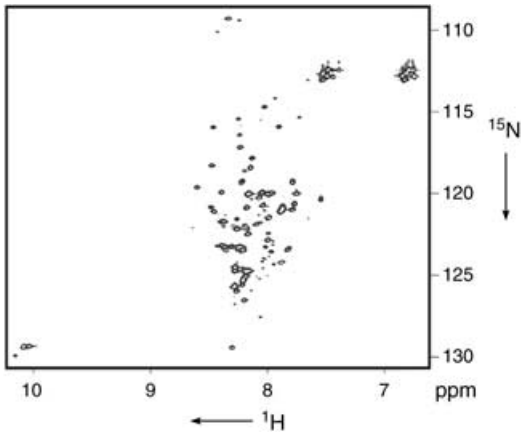

Figure 17. ^{15}N-HSQC spectrum of ^{15}N-labeled Np53. The ^{15}N-HSQC spectrum of the N-terminal domain of human p53 (1.2 mM) was determined at 298 K and pH 7.5 in 90% H_2O/10% D_2O at 750 MHz. Adapted from ref. [123].

In order to corroborate the hydrodynamic properties of the N-terminal domain of p53, pulsed-field gradient diffusion measurements were performed and the data were compared to theoretical hydrodynamic calculations performed by using the bead model of HYDRONMR[120] and a regularized random-coil structure, which was generated by XPLOR.[121] The diffusion coefficient of Np53 was calculated from the decay of 23 nonexchangeable signals, which were averaged and fitted by using the equation of Stejskal and Tanner.[24] The experimental diffusion coefficient was $6.5\times10^{-11}\pm0.05\times10^{-11}$ m^2s^{-1}. This value is in good agreement with the one calculated by using HYDRONMR, namely $D_{thr}=7.43\times10^{-11}$ m^2s^{-1} (Figure 18). The diffusion coefficient is about two times smaller than for a globular folded protein of the same size. This is due to an increased hydrodynamic radius, corresponding to a globular protein of about 20 kDa. Thus, the hydrodynamic calculation together with the NMR diffusion experiments support the idea of an unfolded state of Np53 under physiological conditions.

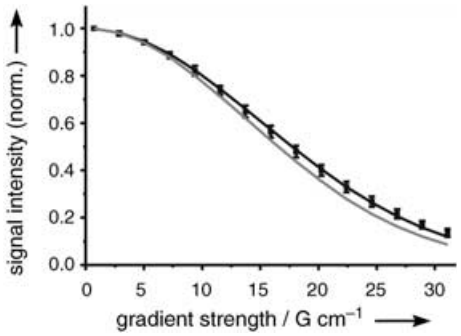

Figure 18. Pulsed-field gradient diffusion experiment of Np53. The squares represent experimental values with increasing gradient strength. Error bars are the result of an average of 23 convergent signal decays of nonexchangeable protons. The nonlinear curve fitting with the Stejskal–Tanner equation[24] is shown as a black line. The gray line represents the signal decay for a regularized extended model structure of Np53 expected from the theoretical diffusion coefficient calculated by HYDRONMR. Adapted from ref. [123]

The N-terminal domain of p53 seems to play an essential role in the regulation of the p53 network. However, the structure and precise function of this domain are still not known. The suggestion that segments of the N-terminal part of p53 could be unfolded in the native state has important implications for the functional mechanism of p53.[122]

^{15}N-HSQC NMR spectra as well as far-UV CD spectroscopy demonstrate that Np53 lacks extensive contributions of ordered secondary structure.[123] Near-UV CD and fluorescence emission spectra of Np53 confirm a high main-chain flexibility in the domain and a complete absence of tertiary structure.[123] The hydrodynamic dimensions of Np53 are typical for a protein of low compactness and an extended conformation under physiological conditions. In addition, the diffusion coefficient obtained by PFG NMR spectroscopy is about two times smaller than the one expected for a globular folded protein of the same size. Both characteristics are in line with the concept of an unfolded conformation of the N-terminal part of p53 under physiological conditions.

Summary

Pulsed-field gradient NMR spectroscopy is a well-established method for the determination of translational diffusion coefficients. Besides the concept of diffusion-ordered spectroscopy (DOSY),[55] which generates a new "diffusion dimension" in the spectra, there are several more applications in the field of biomolecular NMR spectroscopy. Diffusion-based NMR methodologies have been reported for the observation of ligand–receptor interactions,[124,125] the determination of association constants,[126] or the screening of compound mixtures to detect binding ligands.[127] Furthermore, solvation phenomena[128] as well as membrane association can be studied.[129] Studies of the molecular aggregation and hydrodynamic properties of various proteins and peptides[93,130] demonstrated that monomer–dimer equilibria can be determined by pulsed-field gradient NMR methods. Moreover, it is possible to observe the folding of proteins[131,132] and to determine chemical exchange rates by diffusion NMR spectroscopy.[61,133,134] Therefore, pulsed-field gradient diffusion measurements are of considerable value in conformational and hydrodynamic studies of molecules, and "diffusion" can be rightfully added to the more conventional NMR parameters, such as chemical shifts, NOEs, and scalar or dipolar couplings.

Acknowledgements

Financial support by the Deutsche Forschungsgemeinschaft and the Fonds der Chemischen Industrie is gratefully acknowledged.

Keywords: diffusion · molecular interactions · NMR spectroscopy · peptides · proteins

[1] P. Aloy, B. Bottcher, H. Ceulemans, C. Leutwein, C. Mellwig, S. Fischer, A. C. Gavin, P. Bork, G. Superti-Furga, L. Serrano, R. B. Russell, *Science* **2004**, *303*, 2026.

[2] L. Giot, J. S. Bader, C. Brouwer, A. Chaudhuri, B. Kuang, Y. Li, Y. L. Hao, C. E. Ooi, B. Godwin, E. Vitols, G. Vijayadamodar, P. Pochart, H. Machineni, M. Welsh, Y. Kong, B. Zerhusen, R. Malcolm, Z. Varrone, A. Collis, M. Minto, S. Burgess, L. McDaniel, E. Stimpson, F. Spriggs, J. Williams, K. Neurath, N. Ioime, M. Agee, E. Voss, K. Furtak, R. Renzulli, N. Aanensen, S. Carrolla, E. Bickelhaupt, Y. Lazovatsky, A. DaSilva, J. Zhong, C. A. Stanyon, R. L. Finley, K. P. White, M. Braverman, T. Jarvie, S. Gold, M. Leach, J. Knight, R. A. Shimkets, M. P. McKenna, J. Chant, J. M. Rothberg, *Science* **2003**, *302*, 1727.

[3] M. A. Huynen, B. Snel, C. von Mering, P. Bork, *Curr. Opin. Cell Biol.* **2003**, *15*, 191.

[4] A. C. Gavin, G. Superti-Furga, *Curr. Opin. Chem. Biol.* **2003**, *7*, 21.

[5] A. C. Gavin, M. Bosche, R. Krause, P. Grandi, M. Marzioch, A. Bauer, J. Schultz, J. M. Rick, A. M. Michon, C. M. Cruciat, M. Remor, C. Hofert, M. Schelder, M. Brajenovic, H. Ruffner, A. Merino, K. Klein, M. Hudak, D. Dickson, T. Rudi, V. Gnau, A. Bauch, S. Bastuck, B. Huhse, C. Leutwein, M. A. Heurtier, R. R. Copley, A. Edelmann, E. Querfurth, V. Rybin, G. Drewes, M. Raida, T. Bouwmeester, P. Bork, B. Seraphin, B. Kuster, G. Neubauer, G. Superti-Furga, *Nature* **2002**, *415*, 141.

[6] Y. Ho, A. Gruhler, A. Heilbut, G. D. Bader, L. Moore, S. L. Adams, A. Millar, P. Taylor, K. Bennett, K. Boutilier, L. Y. Yang, C. Wolting, I. Donaldson, S. Schandorff, J. Shewnarane, M. Vo, J. Taggart, M. Goudreault, B. Muskat, C. Alfarano, D. Dewar, Z. Lin, K. Michalickova, A. R. Willems, H. Sassi, P. A. Nielsen, K. J. Rasmussen, J. R. Andersen, L. E. Johansen, L. H. Hansen, H. Jespersen, A. Podtelejnikov, E. Nielsen, J. Crawford, V. Poulsen, B. D. Sorensen, J. Matthiesen, R. C. Hendrickson, F. Gleeson, T.

Pawson, M. F. Moran, D. Durocher, M. Mann, C. W. V. Hogue, D. Figeys, M. Tyers, *Nature* **2002**, *415*, 180.
[7] T. Ito, T. Chiba, R. Ozawa, M. Yoshida, M. Hattori, Y. Sakaki, *Proc. Natl. Acad. Sci. USA* **2001**, *98*, 4569.
[8] P. Uetz, L. Giot, G. Cagney, T. A. Mansfield, R. S. Judson, J. R. Knight, D. Lockshon, V. Narayan, M. Srinivasan, P. Pochart, A. Qureshi-Emili, Y. Li, B. Godwin, D. Conover, T. Kalbfleisch, G. Vijayadamodar, M. J. Yang, M. Johnston, S. Fields, J. M. Rothberg, *Nature* **2000**, *403*, 623.
[9] W. S. Price, *Concepts Magn. Reson.* **1998**, *10*, 197.
[10] W. S. Price, *Concepts Magn. Reson.* **1997**, *9*, 299.
[11] M. E. Moseley, Y. Cohen, J. Mintorovitch, L. Chileuitt, H. Shimizu, J. Kucharczyk, M. F. Wendland, P. R. Weinstein, *Magn. Reson. Med.* **1990**, *14*, 330.
[12] P. J. Basser, *NMR Biomed.* **1995**, *8*, 333.
[13] A. G. Palmer, *Curr. Opin. Struct. Biol.* **1997**, *7*, 732.
[14] V. Y. Orekhov, D. M. Korzhnev, K. V. Pervushin, E. Hoffmann, A. S. Arseniev, *J. Biomol. Struct. Dyn.* **1999**, *17*, 157.
[15] S. L. Talagala, I. J. Lowe, *Concepts Magn. Reson.* **1991**, *3*, 145.
[16] Y. Xia, *Concepts Magn. Reson.* **1996**, *8*, 205.
[17] W. S. Price, *NMR Imaging*, Academic Press, London, **1997**.
[18] D. Canet, M. Décorps in *Dynamics of Solutions and Fluid Mixtures* (Ed.: J.-J. Delpuech), Wiley, New York, **1995**, p. 309.
[19] D. Canet, *Prog. Nucl. Magn. Reson. Spectrosc.* **1997**, *30*, 101.
[20] D. Canet in *Encyclopedia of Nuclear Magnetic Resonance* (Eds.: D. M. Grant, R. K. Harris), Wiley, New York, **1996**, p. 3938.
[21] E. L. Hahn, *Phys. Rev.* **1950**, *80*, 580.
[22] H. Y. Carr, E. M. Purcell, *Phys. Rev.* **1954**, *94*, 630.
[23] E. O. Stejskal, *J. Chem. Phys.* **1965**, *43*, 3597.
[24] E. O. Stejskal, J. E. Tanner, *J. Chem. Phys.* **1965**, *42*, 288.
[25] J. E. Tanner, E. O. Stejskal, *J. Chem. Phys.* **1968**, *49*, 1768.
[26] A. Jerschow, N. Müller, *J. Magn. Reson.* **1997**, *125*, 372.
[27] A. Jerschow, *J. Magn. Reson.* **2000**, *145*, 125.
[28] A. Abragam, *The Principles of Nuclear Magnetism*, Clarendon Press, Oxford, **1961**.
[29] H. C. Torrey, *Phys. Rev.* **1956**, *104*, 563.
[30] D. E. Woessner, *J. Chem. Phys.* **1961**, *34*, 2057.
[31] J. E. Tanner, *J. Chem. Phys.* **1970**, *52*, 2523.
[32] D. Burstein, *Concepts Magn. Reson.* **1996**, *8*, 269.
[33] L. E. Kay, J. H. Prestegard, *J. Magn. Reson.* **1986**, *67*, 103.
[34] F. Ferrage, M. Zoonens, D. E. Warschawski, J. L. Popot, G. Bodenhausen, *J. Am. Chem. Soc.* **2003**, *125*, 2541.
[35] A. J. Dingley, J. P. Mackay, G. L. Shaw, B. D. Hambly, G. F. King, *J. Biomol. NMR* **1997**, *10*, 1.
[36] W. S. Price, W.-T. Chang, W.-M. Kwok, L.-P. Hwang, *J. Chin. Chem. Soc.* **1994**, *41*, 119.
[37] W. S. Price in *Annual Reports on NMR Spectroscopy, Vol.* 35 (Ed.: G. A. Webb), Academic Press, London, **1996**, p. 51.
[38] M. Buszko, G. E. Maciel, *J. Magn. Reson. Ser. A* **1994**, *107*, 151.
[39] P. Mansfield, B. Chapman, *J. Phys. E* **1986**, *19*, 540.
[40] P. Mansfield, B. Chapman, *J. Magn. Reson.* **1986**, *66*, 573.
[41] B. Chapman, P. Mansfield, *J. Phys. D* **1986**, *19*, L129.
[42] M. Burl, I. R. Young in *Encyclopedia of Nuclear Magnetic Resonance, Vol.* 3 (Eds.: D. M. Grant, R. K. Harris), Wiley, New York, **1996**, p. 1841.
[43] P. Jehenson, M. Westphal, N. Schuff, *J. Magn. Reson.* **1990**, *90*, 264.
[44] J. J. Vanvaals, A. H. Bergman, *J. Magn. Reson.* **1990**, *90*, 52.
[45] P. D. Majors, J. L. Blackley, S. A. Altobelli, A. Caprihan, E. Fukushima, *J. Magn. Reson.* **1990**, *87*, 548.
[46] S. J. Gibbs, C. S. Johnson, *J. Magn. Reson.* **1991**, *93*, 395.
[47] M. I. Hrovat, C. G. Wade, *J. Magn. Reson.* **1981**, *44*, 62.
[48] M. I. Hrovat, C. G. Wade, *J. Magn. Reson.* **1981**, *45*, 67.
[49] E. Vonmeerwall, M. Kamat, *J. Magn. Reson.* **1989**, *83*, 309.
[50] G. Wider, V. Dotsch, K. Wüthrich, *J. Magn. Reson. Ser. A* **1994**, *108*, 255.
[51] M. D. Pelta, H. Barjat, G. A. Morris, A. L. Davis, S. J. Hammond, *Magn. Reson. Chem.* **1998**, *36*, 706.
[52] A. D. Chen, C. S. Johnson, M. Lin, M. J. Shapiro, *J. Am. Chem. Soc.* **1998**, *120*, 9094.
[53] R. F. Karlicek, I. J. Lowe, *J. Magn. Reson.* **1980**, *37*, 75.
[54] R. M. Cotts, M. J. R. Hoch, T. Sun, J. T. Markert, *J. Magn. Reson.* **1989**, *83*, 252.
[55] C. S. Johnson, Jr., *Prog. Nucl. Magn. Reson. Spectrosc.* **1999**, *34*, 203.
[56] W. S. Price, P. W. Kuchel, *J. Magn. Reson.* **1991**, *94*, 133.
[57] J. Lounila, K. Oikarinen, P. Ingman, J. Jokisaari, *J. Magn. Reson. Ser. A* **1996**, *118*, 50.
[58] P. T. Callaghan, *Principles of Nuclear Magnetic Resonance Microscopy*, Oxford University Press, Oxford, **1993**.
[59] A. D. Bain, *Prog. Nucl. Magn. Reson. Spectrosc.* **2003**, *43*, 63.
[60] C. S. Johnson, *Advances in Magnetic Resonance*, Academic Press, New York, **1965**.
[61] C. S. Johnson, *J. Magn. Reson. Ser. A* **1993**, *102*, 214.
[62] M. F. Lin, M. J. Shapiro, J. R. Wareing, *J. Org. Chem.* **1997**, *62*, 8930.
[63] T. S. Derrick, E. F. McCord, C. K. Larive, *J. Magn. Reson.* **2002**, *155*, 217.
[64] C. S. Johnson, *Nuclear Magnetic Resonance Probes of Molecular Dynamics*, Kluwer Academic, Dordrecht, **1994**.
[65] S. W. Provencher, *J. Chem. Phys.* **1976**, *64*, 2773.
[66] S. W. Provencher, *Biophys. J.* **1976**, *16*, 27.
[67] S. W. Provencher, R. H. Vogel, *Numerical Treatment of Inverse Problems in Differential and Integral Equations*, Birkhauser, Boston, **1983**.
[68] K. F. Morris, C. S. Johnson, *J. Am. Chem. Soc.* **1993**, *115*, 4291.
[69] M. A. Delsuc, T. E. Malliavin, *Anal. Chem.* **1998**, *70*, 2146.
[70] D. H. Wu, A. Chen, C. S. Johnson, *J. Magn. Reson. Ser. A* **1996**, *123*, 215.
[71] D. H. Wu, A. Chen, C. S. Johnson, *J. Magn. Reson. Ser. A* **1996**, *121*, 88.
[72] A. Bax, R. H. Griffey, B. L. Hawkins, *J. Magn. Reson.* **1983**, *55*, 301.
[73] G. Bodenhausen, D. J. Ruben, *Chem. Phys. Lett.* **1980**, *69*, 185.
[74] A. Jerschow, N. Müller, *J. Magn. Reson. Ser. A* **1996**, *123*, 222.
[75] E. K. Gozansky, D. G. Gorenstein, *J. Magn. Reson. Ser. B* **1996**, *111*, 94.
[76] E. L. Cussler, *Diffusion: Mass Transfer in Fluid Systems*, Cambridge University Press, Cambridge, **1984**.
[77] J. Crank, *The Mathematics of Diffusion*, 2nd ed., Clarendon Press, Cambridge, **1975**.
[78] C. R. Cantor, P. R. Schimmel in *Biophysical Chemistry, Part II: Techniques for the Study of Biological Structure and Function, Vol.* II (Ed.: W. H. Freeman), New York, **1980**, p. 570.
[79] B. Halle, V. P. Denisov in *Nuclear Magnetic Resonance of Biological Macromolecules, Part A*, **2001**, p. 178.
[80] K. Modig, E. Liepinsh, G. Otting, B. Halle, *J. Am. Chem. Soc.* **2004**, *126*, 102.
[81] G. Otting, *Prog. Nucl. Magn. Reson. Spectrosc.* **1997**, *31*, 259.
[82] K. Wüthrich, M. Billeter, P. Güntert, P. Luginbuhl, R. Riek, G. Wider, *Faraday Discuss.* **1996**, 245.
[83] V. A. Bloomfield, W. O. Dalton, K. E. V. Holde, *Biopolymers* **1967**, *5*, 149.
[84] V. A. Bloomfield, W. O. Dalton, K. E. V. Holde, *Biopolymers* **1967**, 135.
[85] J. Riseman, J. G. Kirkwood, *J. Chem. Phys.* **1950**, *18*, 512.
[86] J. García de la Torre, M. L. Huertas, B. Carrasco, *Biophys. J.* **2000**, *78*, 719.
[87] J. García de la Torre, *Hydrodynamic Properties of Macromolecular Assemblies*, Cambridge University Press, Cambridge, **1989**.
[88] J. García de la Torre, V. A. Bloomfield, *Biopolymers* **1977**, *16*, 1747.
[89] F. Formaggio, M. Crisma, P. Rossi, P. Scrimin, B. Kaptein, Q. B. Broxterman, J. Kamphuis, C. Toniolo, *Chem. Eur. J.* **2000**, *6*, 4498.
[90] R. Gratias, R. Konat, H. K. M. Crisma, G. Valle, A. Polese, F. Formaggio, C. Toniolo, Q. B. Broxterman, J. Kamphuis, *J. Am. Chem. Soc.* **1998**, *120*, 4763.
[91] C. Toniolo, M. Crisma, F. Formaggio, G. Cavicchioni, G. Precigoux, A. Aubry, J. Kamphuis, *Biopolymers* **1993**, *33*, 1061.
[92] I. L. Karle, P. Balaram, *Biochemistry* **1990**, *29*, 6747.
[93] A. Dehner, E. Planker, G. Gemmecker, Q. B. Broxterman, W. Bisson, F. Formaggio, M. Crisma, C. Toniolo, H. Kessler, *J. Am. Chem. Soc.* **2001**, *123*, 6678.
[94] K. R. MacKenzie, D. M. Engelman, *Proc. Natl. Acad. Sci. USA* **1998**, *95*, 3583.
[95] I. L. Karle, *Acta Crystallogr. Ser. B* **1992**, *48*, 341.
[96] J.-L. Popot, D. M. Engelman, *Biochemistry* **1990**, *29*, 4031.
[97] M. Karplus, D. L. Weaver, *Nature* **1976**, *260*, 404.
[98] A. J. Levine, *Cell* **1997**, *88*, 323.
[99] P. May, E. May, *Oncogene* **1999**, *18*, 7621.
[100] B. Vogelstein, D. Lane, A. J. Levine, *Nature* **2000**, *408*, 307.
[101] K. Vousden, *Br. J. Cancer* **2003**, *88*, S7.
[102] K. H. Vousden, *Cell* **2000**, *103*, 691.
[103] C. P. Rubbi, J. Milner, *EMBO J.* **2003**, *22*, 6068.
[104] R. L. Weinberg, D. B. Veprintsev, A. R. Fersht, *J. Mol. Biol.* **2004**, *341*, 1145.

[105] C. Klein, G. Georges, A. P. Künkele, R. Huber, R. A. Engh, S. Hansen, *J. Biol. Chem.* **2001**, *276*, 37390.
[106] C. Klein, E. Planker, T. Diercks, H. Kessler, K. P. Künkele, K. Lang, S. Hansen, M. Schwaiger, *J. Biol. Chem.* **2001**, *276*, 49020.
[107] K. G. McLure, P. W. K. Lee, *EMBO J.* **1999**, *18*, 763.
[108] K. G. McLure, P. W. K. Lee, *EMBO J.* **1998**, *17*, 3342.
[109] A. K. Nagaich, V. B. Zhurkin, S. R. Durell, R. L. Jernigan, E. Appella, R. E. Harrington, *Proc. Natl. Acad. Sci. USA* **1999**, *96*, 1875.
[110] C. H. Arrowsmith, P. Morin, *Oncogene* **1996**, *12*, 1379.
[111] Y. Cho, S. Gorina, P. D. Jeffrey, N. P. Pavletich, *Science* **1994**, *265*, 346.
[112] A. Lebrun, R. Lavery, H. Weinstein, *Protein Eng.* **2001**, *14*, 233.
[113] C. Prives, *Cell* **1994**, *78*, 543.
[114] K. H. Zhao, X. M. Chai, K. Johnston, A. Clements, R. Marmorstein, *J. Biol. Chem.* **2001**, *276*, 12120.
[115] W. T. Lee, T. S. Harvey, Y. Yin, P. Yau, D. Litchfield, C. H. Arrowsmith, *Nat. Struct. Biol.* **1994**, *1*, 877.
[116] P. D. Jeffrey, S. Gorina, N. P. Pavletich, *Science* **1995**, *267*, 1498.
[117] G. M. Clore, J. Ernst, R. Clubb, J. G. Omichinski, W. M. Kennedy, K. Sakaguchi, E. Appella, A. M. Gronenborn, *Nat. Struct. Biol.* **1995**, *2*, 321.
[118] T. M. Rippin, S. M. V. Freund, D. B. Veprintsev, A. R. Fersht, *J. Mol. Biol.* **2002**, *319*, 351.
[119] J. García de la Torre, M. L. Huertas, B. Carrasco, *J. Magn. Reson.* **2000**, *147*, 138.
[120] J. García de la Torre, M. L. Huertas, B. Carrasco, *J. Magn. Reson.* **2000**, *147*, 138.
[121] A. T. Brünger, *X-PLOR Version 3.1: A System for X-ray Crystallography and NMR*, Yale University Press, New Haven, CT, **1992**.
[122] S. Bell, C. Klein, L. Müller, S. Hansen, J. Buchner, *J. Mol. Biol.* **2002**, *322*, 917.
[123] R. Dawson, L. Müller, A. Dehner, C. Klein, H. Kessler, J. Buchner, *J. Mol. Biol.* **2003**, *332*, 1131.
[124] T. S. Derrick, L. H. Lucas, J.-L. Dimicoli, C. K. Larive, *Magn. Reson. Chem.* **2002**, *40*, S98.
[125] H. Ponstingle, G. Otting, *J. Biomol. NMR* **1997**, *9*, 441.
[126] O. Mayzel, Y. Cohen, *J. Chem. Soc. Chem. Commun.* **1994**, 1901.
[127] K. Bleicher, M. Lin, M. J. Shapiro, J. R. Wareing, *J. Org. Chem.* **1998**, *63*, 8486.
[128] M. Fioroni, M. D. Diaz, K. Burger, S. Berger, *J. Am. Chem. Soc.* **2002**, *124*, 7737.
[129] A. R. Waldeck, P. W. Kuchel, A. J. Lennon, B. E. Chapman, *Prog. Nucl. Magn. Reson. Spectrosc.* **1997**, *30*, 39.
[130] X. Chang, D. Keller, S. I. O'Donoghue, J. J. Led, *FEBS Lett.* **2002**, *515*, 165.
[131] J. A. Jones, D. K. Wilkins, L. J. Smith, C. M. Dobson, *J. Biomol. NMR* **1997**, *10*, 199.
[132] J. Balbach, *J. Am. Chem. Soc.* **2000**, *122*, 5887.
[133] A. Chen, C. S. Johnson, M. Lin, M. J. Shapiro, *J. Am. Chem. Soc.* **1998**, *120*, 9094.
[134] M. Liu, H. C. Toms, G. E. Hawkes, J. K. Nicholson, J. C. Lindon, *J. Biomol. NMR* **1999**, *13*, 25.
[135] A. Dehner, C. Klein, S. Hansen, L. Müller, J. Buchner, M. Schwaiger, H. Kessler, *Angew. Chem.* **2005**, *117*, 5381–5386; *Angew. Chem. Int. Ed.* **2005**, *44*, 5247–5251.

Received: March 10, 2005

